

## Introduction

The use of radioactive isotopes for medical purposes has been investigated since 1920, and since 1940 attempts have been undertaken to image radionuclide concentration in the human body. In the early 1950s, Ben Cassen introduced the rectilinear scanner, a “zero-dimensional” scanner, which (very) slowly scanned in two dimensions to produce a projection image, like a radiograph, but this time of the radionuclide concentration in the body. In the late 1950s, Hal Anger developed the first “true” gamma camera, introducing an approach that is still being used in the design of all modern cameras: the Anger scintillation camera [21], a 2D planar detector to produce a 2D projection image without scanning.

The Anger camera can also be used for tomography. The projection images can then be used to compute the original spatial distribution of the radionuclide within a slice or a volume, in a process similar to reconstruction in X-ray computed tomography. Already in 1917, Radon published the mathematical method for reconstruction from projections, but only in the 1970s was the method applied in medical applications – first to CT, and then to nuclear medicine imaging. At the same time, iterative reconstruction methods were being investigated, but the application of those methods had to wait until the 1980s for sufficient computer power.

The preceding tomographic system is called a *SPECT* scanner. SPECT stands for single-photon emission computed tomography. Anger also showed that two scintillation cameras could be combined to detect *photon pairs* originating after positron emission. This principle is the basis of *PET* (i.e., positron emission tomography), which detects photon pairs. Ter-Pogossian *et al.* built the first dedicated PET system in the 1970s, which was used for phantom

[21] S. R. Cherry, J. Sorenson, and M. Phelps. *Physics in Nuclear Medicine*. Philadelphia, PA: W. B. Saunders Company, 3rd edition, 2003.

studies. Soon afterward, Phelps, Hoffman *et al.* built the first PET scanner (also called PET camera) for human studies [22]. The PET camera has long been considered almost exclusively as a research system. Its breakthrough as a clinical instrument dates only from the last decade.

## Radionuclides

In nuclear medicine, a tracer molecule is administered to the patient, usually by intravenous injection. A tracer is a particular molecule carrying an unstable isotope – a *radionuclide*. In the body this molecule is involved in a metabolic process. Meanwhile the unstable isotopes emit  $\gamma$ -rays, which allow us to measure the concentration of the tracer molecule in the body as a function of position and time. Consequently, in nuclear medicine the function or metabolism is measured. With CT, MRI, and ultrasound imaging, functional images can also be obtained, but nuclear medicine imaging provides measurements with an SNR that is orders of magnitude higher than that of any other modality.

## Radioactive decay modes

During its radioactive decay a radionuclide loses energy by emitting radiation in the form of particles and electromagnetic rays. These rays are called  $\gamma$ -rays or X-rays. In nuclear medicine, the photon energy ranges roughly from 60 to 600 keV. Usually, electromagnetic rays that originate from nuclei are called  $\gamma$ -rays, although they fall into the same frequency range as X-rays and are therefore indistinguishable.

There are many ways in which a radionuclide can decay. In general, the radioactive decay modes can be subdivided into two main categories: decays

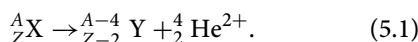
[22] M. Ter-Pogossian. Instrumentation for cardiac positron emission tomography: background and historical perspective. In S. Bergmann and B. Sobel, editors, *Positron Emission Tomography of the Heart*. New York: Futura Publishing Company, 1992.

with emission or capture of nucleons, i.e., neutrons and protons, and decays with emission or capture of  $\beta$ -particles, i.e, electrons and positrons.

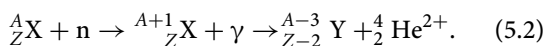
### Nucleon emission or capture

Nucleon emission or capture is not used in imaging because these particles cause heavy damage to tissue due to their high kinetic energy. Instead they can be used in radiotherapy for tumor irradiation.

An example is neutron capture therapy, which exploits the damaging properties of  $\alpha$ -particles. An  $\alpha$ -particle is a helium nucleus, which consists of two protons and two neutrons. It results from the decay of an unstable atom X into atom Y as follows:



If X has mass number\* A and atomic number† Z, then Y has mass number A – 4 and atomic number Z – 2. The  $\alpha$ -particle  ${}^4_2 He^{2+}$  is a heavy particle with a typical kinetic energy of 3–7 MeV. This kinetic energy is rapidly released when interacting with tissue. The range of an  $\alpha$ -particle is only 0.01 to 0.1 mm in water and soft tissue. In order to irradiate a deeply located tumor, neutron capture therapy can be applied. Neutrons, produced by a particle accelerator, penetrate deeply into the tissue until captured by a chemical component injected into the tumor. At that moment  $\alpha$ -particles are released:



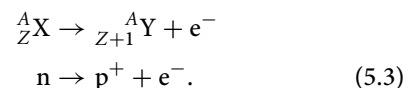
The radioactive decay modes discussed below are all used in nuclear medicine imaging. Depending on the decay mode, a  $\beta$ -particle is emitted or captured and one or a pair of  $\gamma$ -rays is emitted in each event.

\* The mass number is the sum of the number of nucleons, i.e., neutrons and protons.

† The atomic number is the number of protons. Isotopes of a chemical element have the same atomic number (number of protons in the nucleus) but have different mass numbers (from having different numbers of neutrons in the nucleus). Examples are  ${}^{12}_6 C$  and  ${}^{14}_6 C$  (6 protons and 6 respectively 8 neutrons). Different isotopes of the same element cannot have the same mass number, but isotopes of different elements often do have the same mass number. Examples are  ${}^{99}_{47} Mo$  and  ${}^{99}_{45} Tc$ ,  ${}^{14}_6 C$  (6 protons and 8 neutrons) and  ${}^{14}_7 N$  (7 protons and 7 neutrons).

### Electron $\beta^-$ emission

In this process, a neutron is transformed essentially into a proton and an electron (called a  $\beta^-$ -particle):



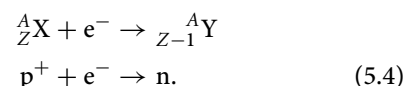
Because the number of protons is increased, this transmutation process corresponds to a rightward step in Mendelejev's table.

In some cases the resulting daughter product of the preceding transmutation can still be in a *metastable* state  ${}^{Am}_{Z-1} Y$ . In that case it decays further with a certain delay to a more stable nuclear arrangement, releasing the excess energy as one or more  $\gamma$ -photons. The nucleons are unchanged, thus there is no additional transmutation in decay from excited to ground state.

Because  $\beta$ -particles damage the tissue and have no diagnostic value, preference in imaging is given to metastable radionuclides, which are pure sources of  $\gamma$ -rays. The most important single-photon tracer,  ${}^{99m}_{43} Tc$ , is an example of this mode.  ${}^{99m}_{43} Tc$  is a metastable daughter product of  ${}^{99}_{45} Mo$  (half-life = 66 hours).  ${}^{99m}_{43} Tc$  decays to  ${}^{99}_{43} Tc$  (half-life = 6 hours) by emitting a photon of 140 keV. The half-life is the time taken to decay to half of its initial quantity.

### Electron capture (EC)

Essentially, an orbital electron is captured and combined with a proton to produce a neutron:

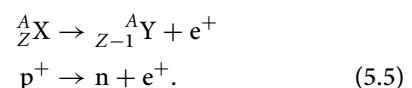


Note that EC causes transmutation toward the left-most neighbor in Mendelejev's table. An example of a single-photon tracer of this kind used in imaging is  ${}^{123}_{53} I$  with a half-life of 13 hours.

The daughter emits additional energy as  $\gamma$ -photons. Similar to  $\beta^-$  emission it can be metastable, which is characterized by a delayed decay.

### Positron emission ( $\beta^+$ decay)

A proton is transformed essentially into a neutron and a positron (or anti-electron):



After a very short time ( $\sim 10^{-9}$  s) and within a few millimeters of the site of its origin, the positron hits an electron and *annihilates* (Figure 5.1). The mass of the two particles is converted into energy, which is emitted as two photons. These photons are emitted in opposite directions. Each photon has an energy of 511 keV, which is the rest mass of an electron or positron. This physical principle is the basis of positron emission tomography (PET). An example of a positron emitter used in imaging is  $^{18}\text{F}$  with a half-life of 109 minutes.

As in  $\beta^-$  emission and EC, the daughter nucleus may further emit  $\gamma$ -photons, but they have no diagnostic purpose in PET.

As a rule of thumb, light atoms tend to emit positrons, and heavy ones tend to prefer other modes, but there are exceptions.

## Statistics

In nuclear medicine imaging, the number of detected photons is generally much smaller than in X-ray

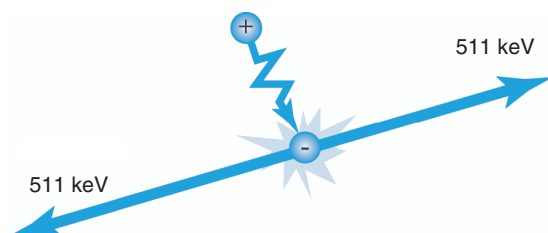


**Figure 5.1** Schematic representation of a positron–electron annihilation. When a positron comes in the neighborhood of an electron, the two particles are converted into a pair of photons, each of 511 keV, which travel in opposite directions.

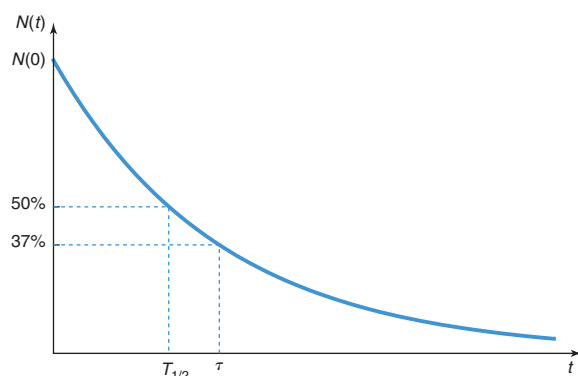


**Figure 5.2** Exponential decay.  $\tau$  is the time constant and  $T_{1/2}$  the half-life.

imaging. Consequently, noise plays a more important role here, and the imaging process is often considered to be stochastic.

The exact moment at which an atom decays cannot be predicted. All that is known is its decay probability per time unit, which is an isotope dependent constant  $\alpha$ . Consequently, the decay per time unit is

$$\frac{dN(t)}{dt} = -\alpha N(t), \quad (5.6)$$

where  $N(t)$  is the number of radioactive isotopes at time  $t$ . Solving this differential equation yields (see Figure 5.2)

$$N(t) = N(t_0)e^{-\alpha(t-t_0)} = N(t_0)e^{-(t-t_0)/\tau}. \quad (5.7)$$

$\tau = 1/\alpha$  is the *time constant* of the exponential decay. Note that  $N(t)$  is the expected value. During a measurement a different value may be found because the process is statistical. The larger  $N$  is, the better the estimate will be. Using Eq. (5.7) and replacing  $t$  by the *half-life*  $T_{1/2}$  and  $t_0$  by 0 yields

$$\begin{aligned} N(T_{1/2}) &= N(0)e^{-T_{1/2}/\tau} = \frac{1}{2}N(0) \\ -T_{1/2}/\tau &= \ln \frac{1}{2} = -\ln 2 \\ T_{1/2} &= \tau \ln 2 = 0.69\tau. \end{aligned} \quad (5.8)$$

Depending on the isotope the half-life varies between fractions of seconds and billions of years.

Note that the presence of radioactivity in the body depends not only on the radioactive decay but also on biological excretion. Assuming a biological half-life  $T_B$ , the effective half-life  $T_E$  can be calculated as

$$\frac{1}{T_E} = \frac{1}{T_B} + \frac{1}{T_{1/2}}. \quad (5.9)$$

Currently the preferred unit of radioactivity is the becquerel (Bq). The curie (Ci) is the older unit.\* One Bq means one expected event per second and  $1 \text{ mCi} = 37 \text{ MBq}$ . Typical doses in imaging are on the order of  $10^2 \text{ MBq}$ .

It can be shown that the probability of measuring  $n$  photons when  $r$  photons are expected, equals

$$p_r(n) = \frac{e^{-r} r^n}{n!}. \quad (5.10)$$

\* Marie and Pierre Curie and Antoine Becquerel received the Nobel Prize in 1903 for their discovery of radioactivity in 1896.

This is a *Poisson distribution* in which  $r$  is the average number of expected photons and  $\sqrt{r}$  is the standard deviation.  $r$  is also the value with the highest probability. Hence, the signal-to-noise ratio (SNR) becomes

$$\text{SNR} = \frac{r}{\sqrt{r}} = \sqrt{r}. \quad (5.11)$$

Obviously, the SNR becomes larger with longer measurements.

For large  $r$ , a Poisson distribution can be well approximated by a Gaussian with the same mean and standard deviation. For small values of  $r$ , the distribution becomes asymmetrical, because the probability is always zero for negative values.

## Interaction of $\gamma$ -photons and particles with matter

### Interaction of particles with matter

Particles, such as  $\alpha$ - and  $\beta$ -particles, interact with tissue by losing their kinetic energy along a straight trajectory through the tissue (Figure 5.3). This straight track is called the range  $R$ . In tissue  $R_\alpha$  is on the order of 0.01 to 0.1 mm, while  $R_\beta$  is typically a few millimeters.

### Interaction of $\gamma$ -photons with matter

As in X-ray imaging, the two most important photon-electron interactions (i.e., Compton scatter and photoelectric absorption) attenuate the emitted  $\gamma$ -rays.

If initially  $N(a)$  photons are emitted in point  $s = a$  along the  $s$ -axis, the number of photons  $N(d)$  in the detector at position  $s = d$  along the  $s$ -axis is

$$N(d) = N(a) e^{-\int_a^d \mu(s) ds}, \quad (5.12)$$

where  $\mu$  is the linear absorption coefficient. Obviously, the attenuation of a photon depends on the position  $s = a$  where it is emitted. Note that it also depends on the attenuating tissue and on the energy of the photons. For example, for photons emitted by  $^{99m}\text{Tc}$

(140 keV) the median of the penetration depth in water is about 4.5 cm.

In PET, a pair of photons of 511 keV each has to be detected. Because both photons travel independently through the tissue, the detection probabilities must be multiplied. Assume that one detector is positioned in  $s = d_1$ , the second one in  $s = d_2$ , and a point source is located in  $s = a$  somewhere between the two detectors. Assume further that during a measurement  $N(a)$  photon pairs are emitted along the  $s$ -axis. The number of detected pairs then is

$$N(d_1, d_2) = N(a) e^{-\int_{d_1}^a \mu(s) ds} e^{-\int_{d_2}^a \mu(s) ds} \\ = N(a) e^{-\int_{d_1}^{d_2} \mu(s) ds}. \quad (5.13)$$

In contrast to SPECT, the attenuation in PET is identical for each point along the projection line.

## Data acquisition

Photon detection hardware in nuclear medicine differs considerably from that used in CT. In CT, a large number of photons must be acquired in a very short measurement. In emission tomography, a very small number of photons is acquired in a longer time interval. Consequently, emission tomography detectors are optimized for sensitivity.

### The detector

#### Detecting the photon

Photomultiplier tubes coupled to a scintillation crystal are still very common today. Newer detectors are *photodiodes*, coupled to a scintillator, and *photoconductors* (e.g., CZT), which directly convert X-ray photons into an electrical conductivity (see also p. 35).

A scintillation crystal absorbs the photon via photoelectric absorption. The resulting electron travels through the crystal while distributing its kinetic energy over a few thousand electrons in multiple collisions. These electrons release their energy in the form of a photon of a few electronvolts. These photons are

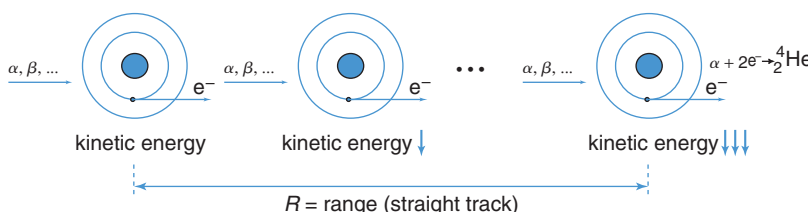


**Figure 5.3** Interaction of particles with matter. The particles are slowed down along a straight track while releasing their kinetic energy.

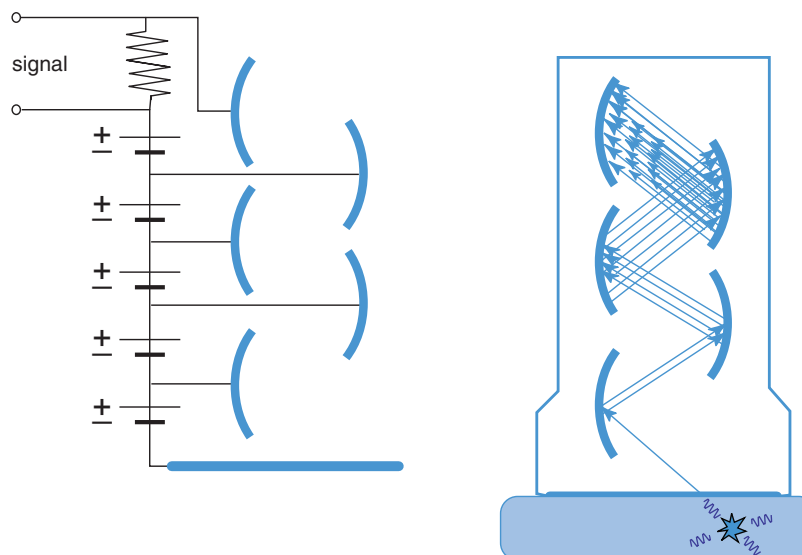


**Figure 5.4** Photomultiplier. Left: the electrical scheme. Right: scintillation photons from the crystal initiate an electric current to the dynode, which is amplified in subsequent stages.

visible to the human eye, which explains the term “scintillation.”

Because the linear attenuation coefficient increases with the atomic number  $Z$  (see Eq. (2.12)), the scintillation crystal must have a high  $Z$ . Also, the higher the photon energy, the higher  $Z$  should be because the probability of interaction decreases with increasing energy. In single-photon imaging,  $^{99m}\text{Tc}$  is the tracer used most often. It has an energy of 140 keV, and the gamma camera performance is often optimized for this energy. Obviously, PET cameras have to be optimized for 511 keV. Many scintillators exist and extensive research on new scintillators is still going on. The crystals that are most often used today are NaI(Tl) for single photons (140 keV) in gamma camera and SPECT, and BGO (bismuth germanate), GSO (gadolinium silicate) and LSO (lutetium oxyorthosilicate) for annihilation photons (511 keV) in PET.

A *photomultiplier tube* (PMT) consists of a photocathode on top, followed by a cascade of dynodes (Figure 5.4). The PMT is glued to the crystal. Because the light photons should reach the photocathode of the PMT, the crystal must be transparent to the visible photons. The energy of the photons hitting the photocathode releases some electrons from the cathode. These electrons are then accelerated toward the positively charged dynode nearby. They arrive with higher energy (the voltage difference  $\times$  the charge), activating additional electrons. Because the voltage becomes systematically higher for subsequent dynodes, the number of electrons increases in every stage,

finally producing a measurable signal. Because the multiplication in every stage is constant, the final signal is proportional to the number of scintillation photons, which in turn is proportional to the energy of the original photon. Hence, a  $\gamma$ -photon is detected, and its energy can also be measured.

### Collimation

In radiography and X-ray tomography, the position of the point source is known and every detected photon provides information about a line that connects the source with the detection point. This is called the projection line. In nuclear medicine, the source has an unknown spatial distribution. Unless some collimation is applied, the detected photons do not contain information about this distribution.

In single-photon detection (SPECT), collimation is done with a mechanical collimator, which is essentially a thick lead plate with small holes (Figure 5.5(a)). The metal plate absorbs all the photons that do not propagate parallel to the axis of the holes. Obviously, most photons are absorbed, and the sensitivity suffers from this approach.

In PET, mechanical collimation is not needed. Both photons are detected with an electronic coincidence circuit (Figure 5.5(b)), and because they propagate in opposite directions, their origin must lie along the line that connects the detection points. This technique is called “coincidence detection” or “electronic collimation.” Although in PET two photons instead of one must resist the absorption process, the

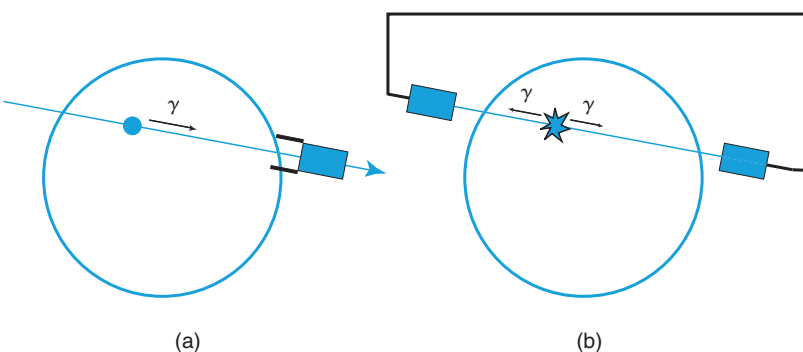


**Figure 5.5** Principle of collimation in (a) SPECT and (b) PET. In SPECT collimation is done with mechanical collimators, while in PET photon pairs are detected by electronic coincidence circuits connecting pairs of detectors.

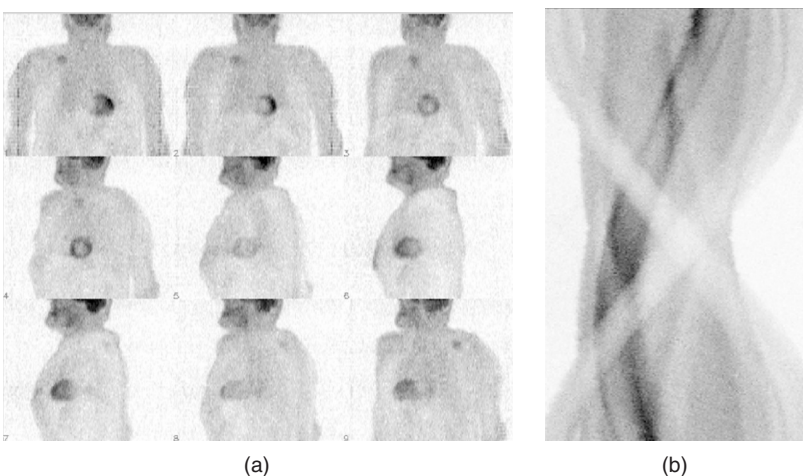


**Figure 5.6** Raw PET data organized as projections (a) and as a sinogram (b). Typically, there are a few hundred projections, one for each projection angle, and about a hundred sinograms, one for each slice through the patient's body. (Courtesy of the Department of Nuclear Medicine.)

sensitivity in PET is higher than that of single-photon imaging systems because no photons are absorbed by a lead collimator.

In summary, both in PET and in SPECT, information about lines is acquired. As in CT, these projection lines are used as input to the reconstruction algorithm. Figure 5.6 shows an example of the raw data, which can be organized as projections or as sinograms.

### Photon position

To increase the sensitivity, the detector area around the patient should be as large as possible. A large detector can be constructed by covering one side of a single large crystal (e.g.,  $50 \times 40 \times 1$  cm) with a dense matrix (30 to 70) of PMTs (a few centimeters width each). Light photons from a single scintillation are picked up by multiple PMTs. The energy is then measured as the sum of all PMT outputs. The position  $(x, y)$  where the

photon hits the detector is recovered as

$$x = \frac{\sum_i x_i S_i}{\sum_i S_i}, \quad y = \frac{\sum_i y_i S_i}{\sum_i S_i}, \quad (5.14)$$

where  $i$  is the PMT index,  $(x_i, y_i)$  the position of the PMT, and  $S_i$  the integral of the PMT output over the scintillation duration. In this case, the spatial resolution is limited by statistical fluctuations in the PMT output.

In a single large crystal design, all PMTs contribute to the detection of a single scintillation. Consequently, two photons hitting the crystal simultaneously yield an incorrect position and energy. Hence, the maximum count rate is limited by the decay time of the scintillation event. Multiple, optically separated, crystal modules (e.g.,  $50 \text{ mm} \times 50 \text{ mm}$ ), connected to a few (e.g.  $2 \times 2$ ) PMTs, offer a solution to this problem. The different modules operate in parallel, this way yielding

much higher count rates than a single crystal design. PET detectors typically use separate crystal modules while in SPECT, where the count rates are typically lower than in PET, most detectors consist of a single large crystal. More details are given in the section on equipment below (p. 117).

## Number of photons detected

Assume a spatial distribution of tracer activity  $\lambda(s)$  along the  $s$ -axis. In Eqs. (5.12) and (5.13),  $N(a)$  must then be replaced by  $\lambda(s) ds$  and integrated along the projection line  $s$ . For SPECT, we obtain

$$N(d) = \int_{-\infty}^{+\infty} \lambda(s) e^{-\int_s^d \mu(\xi) d\xi} ds, \quad (5.15)$$

and for PET,

$$N(d_1, d_2) = e^{-\int_{d_1}^{d_2} \mu(s) ds} \int_{-\infty}^{+\infty} \lambda(s) ds. \quad (5.16)$$

In PET the attenuation is identical for each point along the projection line. Hence, the measured projections are a simple scaling of the unattenuated projections. In SPECT, however, attenuation is position dependent, and no simple relation exists between attenuated and unattenuated projections. Image reconstruction is therefore more difficult in SPECT than in PET, as will be explained on p. 112.

## Energy resolution

As mentioned earlier, an estimate of the energy of the impinging photon is computed by integrating the output of the PMTs. The precision of that estimate is called the “energy resolution.” The number of electrons activated in a scintillation event is subject to statistical noise. The time delay after which each electron releases the scintillation light photon is also a random number. Also, the direction in which these light photons are emitted is unpredictable. Consequently, the PMT output is noisy and limits the energy resolution. The energy resolution is usually quantified as the FWHM of the energy distribution and is expressed as a percentage of the photopeak value. It ranges from 10% FWHM in NaI(Tl) to 15% FWHM in LSO and GSO, to over 20% FWHM in BGO. Hence, the energy resolution is 14 keV for a 140 keV photon detected in NaI(Tl) and 130 keV for a 511 keV photon detected in BGO.

## Count rate

In nuclear medicine, radioactive doses are kept low for the patient because of the long exposure times. The detectors have been designed to measure low activity levels and detect individual photons. On the other hand, these devices cannot be used for high activity levels even if this would be desirable. Indeed, the probability that two or more photons arrive at the same time increases with increasing activity. In that case, the localization electronics compute an incorrect single position somewhere between the actual scintillation points. Fortunately, the camera also computes the total energy, which is higher than normal, and these events are discarded. Hence, a photon can only be detected successfully if no other photon arrives while the first one is being detected. The probability that no other photon arrives can be calculated from the Poisson expression (5.10):

$$p(0|\eta N\tau) = e^{-\eta N\tau}, \quad (5.17)$$

where  $\eta$  represents the overall sensitivity of the camera,  $N$  the activity in becquerels, and  $\tau$  is the detection time in seconds. The detection probability thus decreases exponentially with increasing activity in front of the camera!

Obviously, a high value for  $\eta$  is preferred. Therefore, it is important to keep  $\tau$  as small as possible. The gamma camera and PET camera must therefore process the incoming photons very quickly. For typical medical applications, the current machines are sufficiently fast.

## Imaging

### Planar imaging

Planar images are simply the raw single-photon projection data. Hence, each pixel corresponds to the projection along a line  $s$  (see Eq. (5.15)). Its gray value is proportional to the total amount of attenuated activity along that line. To some extent a planar image can be compared with an X-ray image because all the depth information is lost. Figure 5.7 shows an anterior and posterior whole-body ( $^{99m}\text{Tc-MDP}$ ) image acquired with a dual-head gamma camera.

### Fourier reconstruction and filtered backprojection

Assume a spatial distribution of tracer activity  $\lambda(s)$  along the  $s$ -axis. Hence, the number of detected

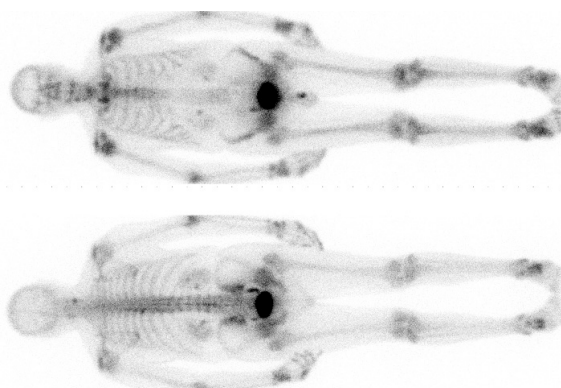


**Figure 5.7**  $^{99m}\text{Tc}$ -MDP study acquired with a dual-head gamma camera. The detector size is about  $40 \times 50$  cm, and the whole-body images are acquired with slow translation of the patient bed. MDP accumulates in bone, yielding images of increased bone metabolism. As a result of the attenuation, the spine is more visible in the lower, posterior image. (Courtesy of Department of Nuclear Medicine.)

photons for SPECT is given by Eq. (5.15) and for PET by Eq. (5.16). In both equations, there is an attenuation factor that prevents straightforward application of Fourier reconstruction or filtered backprojection (which are very successful in CT). For example, at 140 keV, every 5 cm of tissue absorbs about 50% of the photons. Hence, in order to apply the projection theorem, this attenuation effect must be corrected.

In Chapter 3 on CT, we have already seen how to measure and calculate the linear attenuation coefficient  $\mu$  by means of a transmission scan. In order to measure the attenuation, an external radioactive source that rotates around the patient can be used. The SPECT or PET system thus performs a transmission measurement just like a CT scanner. If the external source in position  $d_1$  emits  $N_0$  photons along the  $s$ -axis, the detected fraction of photons at the other side of the patient in position  $d_2$  is

$$\frac{N(d_2)}{N_0} = e^{-\int_{d_1}^{d_2} \mu(s) ds}. \quad (5.18)$$

This is exactly the attenuation factor for PET in Eq. (5.16). It means that a correction for the attenuation in PET can be performed by multiplying the emission measurement  $N(d_1, d_2)$  with the factor  $N_0/N(d_2)$ . Consequently, Fourier reconstruction or filtered backprojection can be applied.

For SPECT, however, this is not possible. In the literature it has been shown that under certain conditions, the projection theorem can still be used

(i.e., if the attenuation is assumed to be a known constant within a convex body contour (such as the head)). Often, a fair body contour can be obtained by segmenting a reconstructed image obtained without attenuation correction. An alternative solution is to use iterative reconstruction, as discussed below. However, in clinical practice, attenuation is often simply ignored, and filtered backprojection is straightforwardly applied. This results in severe reconstruction artifacts. Nevertheless, it turns out that these images still provide very valuable diagnostic information for an experienced physician.

## Iterative reconstruction

The attenuation problem in SPECT is not the only reason to approach the reconstruction as an iterative procedure. Indeed, the actual acquisition data differ considerably from ideal projections because they suffer from a significant amount of Poisson noise, yielding hampering streak artifacts (cf. Figure 3.21(b) for CT).

Several iterative algorithms exist. In this text, a Bayesian description of the problem is assumed, yielding the popular maximum-likelihood (ML) and maximum-a-posteriori (MAP) algorithms. It is further assumed that both the solution and the measurements are discrete values.

### Bayesian approach

Assume that a reconstructed image  $\Lambda$  is computed from the measurement  $Q$ . Bayes' rule states

$$p(\Lambda|Q) = \frac{p(Q|\Lambda)p(\Lambda)}{p(Q)}. \quad (5.19)$$

The function  $p(\Lambda|Q)$  is the posterior probability,  $p(\Lambda)$  the prior probability and  $p(Q|\Lambda)$  the likelihood. Maximizing  $p(\Lambda|Q)$  is called the *maximum-a-posteriori probability* (MAP) approach. It yields the most likely solution given a measurement  $Q$ .

When maximizing  $p(\Lambda|Q)$ , the probability  $p(Q)$  is constant and can be ignored. Because it is not trivial to find good mathematical expressions for the prior probability  $p(\Lambda)$ , it is often also assumed to be constant (i.e., it is assumed that a priori all possible solutions have the same probability to be correct). Maximizing  $p(\Lambda|Q)$  is then reduced to maximizing the likelihood  $p(Q|\Lambda)$ . This is called the *maximum-likelihood* (ML) approach.

### Maximum likelihood (ML)

The measurements  $Q$  are measurements  $q_i$  of the attenuated projections  $r_i$  in detector position  $i$ . The reconstruction image  $\Lambda$  is the regional activity  $\lambda_j$  in each pixel  $j$ . The numerical relation between  $r_i$  and  $\lambda_j$  can be written as

$$r_i = \sum_{j=1,J} c_{ij}\lambda_j, \quad i = 1, I. \quad (5.20)$$

The value  $c_{ij}$  represents the sensitivity of detector  $i$  for activity in  $j$ , which includes the attenuation of the  $\gamma$ -rays from  $j$  to  $i$ . If we have a perfect collimation,  $c_{ij}$  is zero everywhere except for the pixels  $j$  that are intersected by projection line  $i$ , yielding a sparse matrix  $C$ . This notation is very general, and allows us, for example, to take the finite acceptance angle of the mechanical collimator into account, which would increase the fraction of nonzero  $c_{ij}$ . Similarly, if the attenuation is known, it can be taken into account when computing  $c_{ij}$ .

Because it can be assumed that the data are samples from a Poisson distribution, the likelihood of measuring  $q_i$  if  $r_i$  photons on average are expected (see Eq. (5.10)) can be computed as

$$p(q_i|r_i) = \frac{e^{-r_i} r_i^{q_i}}{q_i!}. \quad (5.21)$$

Because the history of one photon (emission, trajectory, possible interaction with electrons, possible detection) is independent of that of the other photons, the overall probability is the product of the individual probabilities:

$$p(Q|\Lambda) = \prod_i \frac{e^{-r_i} r_i^{q_i}}{q_i!}. \quad (5.22)$$

Obviously, this is a very small number: for example, for  $r_i = 15$  the maximum value of  $p(q_i|r_i)$  is 0.1. For larger  $r_i$ , the maximum value of  $p$  is even smaller. In a measurement for a single slice, we have on the order of 10 000 detector positions  $i$ , and the maximum likelihood value is on the order of  $10^{-10\,000}$ .

When calculating the argument  $\Lambda$  that maximizes  $p(Q|\Lambda)$ , the data  $q_i!$  are constant and can be ignored. Hence,

$$\arg \max_{\Lambda} p(Q|\Lambda) = \arg \max_{\Lambda} \prod_i e^{-r_i} r_i^{q_i}. \quad (5.23)$$

Because the logarithm is monotonically increasing, maximizing the log-likelihood function also maximizes  $p(Q|\Lambda)$ , that is,

$$\begin{aligned} \arg \max_{\Lambda} p(Q|\Lambda) &= \arg \max_{\Lambda} \ln p(Q|\Lambda) \\ &= \arg \max_{\Lambda} \sum_i (q_i \ln(r_i) - r_i) \\ &= \arg \max_{\Lambda} \sum_i \left( q_i \ln(\sum_j c_{ij}\lambda_j) - \sum_j c_{ij}\lambda_j \right). \end{aligned} \quad (5.24)$$

It turns out that the Hessian (the matrix of second derivatives) is negative definite if the matrix  $c_{ij}$  has maximum rank. In practice, this means that the likelihood function has a single maximum, provided that a sufficient number of different detector positions  $i$  are used.

To solve Eq. (5.24) and calculate  $\lambda_j$ , the partial derivatives are put to zero:

$$\begin{aligned} \frac{\partial}{\partial \lambda_j} \sum_i &\left( q_i \ln(\sum_j c_{ij}\lambda_j) - \sum_j c_{ij}\lambda_j \right) \\ &= \sum_i c_{ij} \left( \frac{q_i}{\sum_j c_{ij}\lambda_j} - 1 \right) = 0, \quad \forall j = 1, J. \end{aligned} \quad (5.25)$$

This system can be solved iteratively. A popular method with guaranteed convergence is the *expectation-maximization* (EM) algorithm. Although the algorithm is simple, the underlying theory is not and is beyond the scope of this textbook.

Because the amount of radioactivity must be kept low, the number of detected photons is also low, yielding a significant amount of Poisson noise, which strongly deteriorates the projection data. Although the ML-EM algorithm takes Poisson noise into account, it attempts to find the most likely solution, which is an image whose calculated projections are as similar as possible to the measured projections. The consequence is that it converges to a noisy reconstructed image.

To suppress the noise, the measured projections must not be smoothed because this would destroy their Poisson nature used by the reconstruction algorithm. Several alternatives exist as follows.

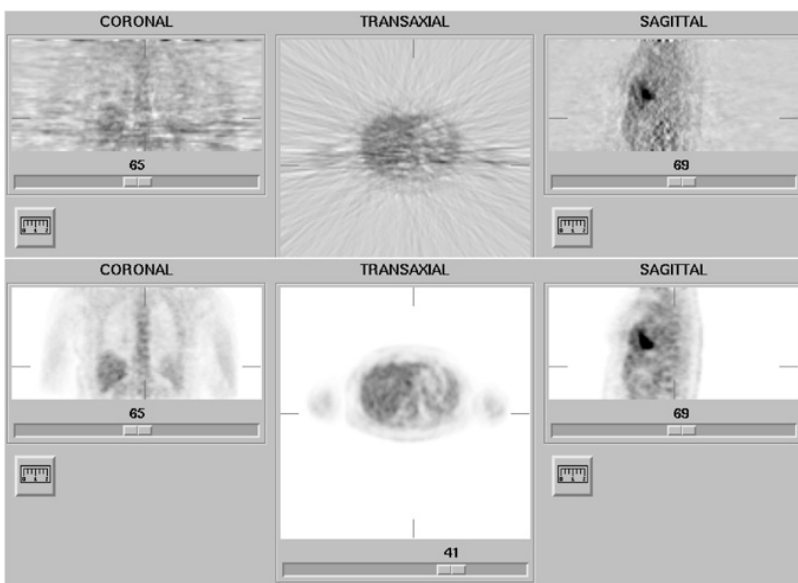


**Figure 5.8** Reconstruction obtained with filtered backprojection (top) and maximum-likelihood expectation-maximization (34 iterations) (bottom). The streak artifacts in the filtered backprojection image are due to the statistical Poisson noise on the measured projection (cf. Figure 3.21(b) for X-ray CT.) (Courtesy of the Department of Nuclear Medicine.)

- The reconstructed image can be smoothed.
- Another approach is to interrupt the iterations before convergence. The ML-EM algorithm has the remarkable characteristic that low frequencies converge faster than high ones. Terminating early has an effect comparable to low-pass filtering. This approach was applied to obtain the image shown in Figure 5.8.
- It is also possible to define some prior probability function that encourages smooth solutions. This yields a *maximum-a-posteriori* (MAP) algorithm, discussed below.

### Maximum-a-posteriori probability (MAP)

The ML approach assumes that the prior probability  $p(\Lambda)$  is constant. Consequently, the argument  $\Lambda$  that maximizes the posterior probability  $p(\Lambda|Q)$  also maximizes the likelihood  $p(Q|\Lambda)$ . However, if prior knowledge of the tracer activity  $\Lambda$  is known, it can be used to improve the quality of the reconstructed image. Starting from Eq. (5.19) the goal then is to find

$$\arg \max_{\Lambda} p(\Lambda|Q) = \arg \max_{\Lambda} (\ln p(Q|\Lambda) + \ln p(\Lambda)) \quad (5.26)$$

where  $\ln p(Q|\Lambda)$  is defined in Eq. (5.24).  $\ln p(\Lambda)$  can be defined as

$$p(\Lambda) = \frac{e^{-E(\Lambda)}}{\sum_{\Lambda} e^{-E(\Lambda)}}. \quad (5.27)$$

where  $E(\Lambda)$  is the so-called Gibbs energy (see also p. 176). Equation (5.26) then becomes

$$\arg \max_{\Lambda} p(\Lambda|Q) = \arg \max_{\Lambda} (\ln p(Q|\Lambda) - E(\Lambda)). \quad (5.28)$$

If, for example, neighboring pixels have similar activity,  $E(\Lambda)$  can be defined as

$$E(\Lambda) = \sum_j \sum_{k \in N_j} \Phi(\lambda_j, \lambda_k) \quad (5.29)$$

where  $N_j$  is a small neighborhood of  $j$  and  $\Phi(\lambda_j, \lambda_k)$  is a function that increases with the amount of dissimilarity between  $\lambda_j$  and  $\lambda_k$ . This way Eq. (5.28) yields a smooth solution.

Prior anatomical knowledge can also be taken into account this way. For example, in Figure 5.9 a high-resolution anatomical image was segmented into different tissue classes (gray matter, white matter, cerebrospinal fluid, etc.) using the method of statistical pixel classification explained in Chapter 7, p. 167. During the iterative reconstruction process it can be required that pixels belonging to the same tissue class have a similar tracer activity. This can be obtained by restricting  $N_j$  in Eq. (5.29) to the local neighborhood of  $j$  with an identical tissue label as that of pixel  $j$ . This way the tracer activity, measured at low resolution, is iteratively forced back within its expected high-resolution tissue boundaries.

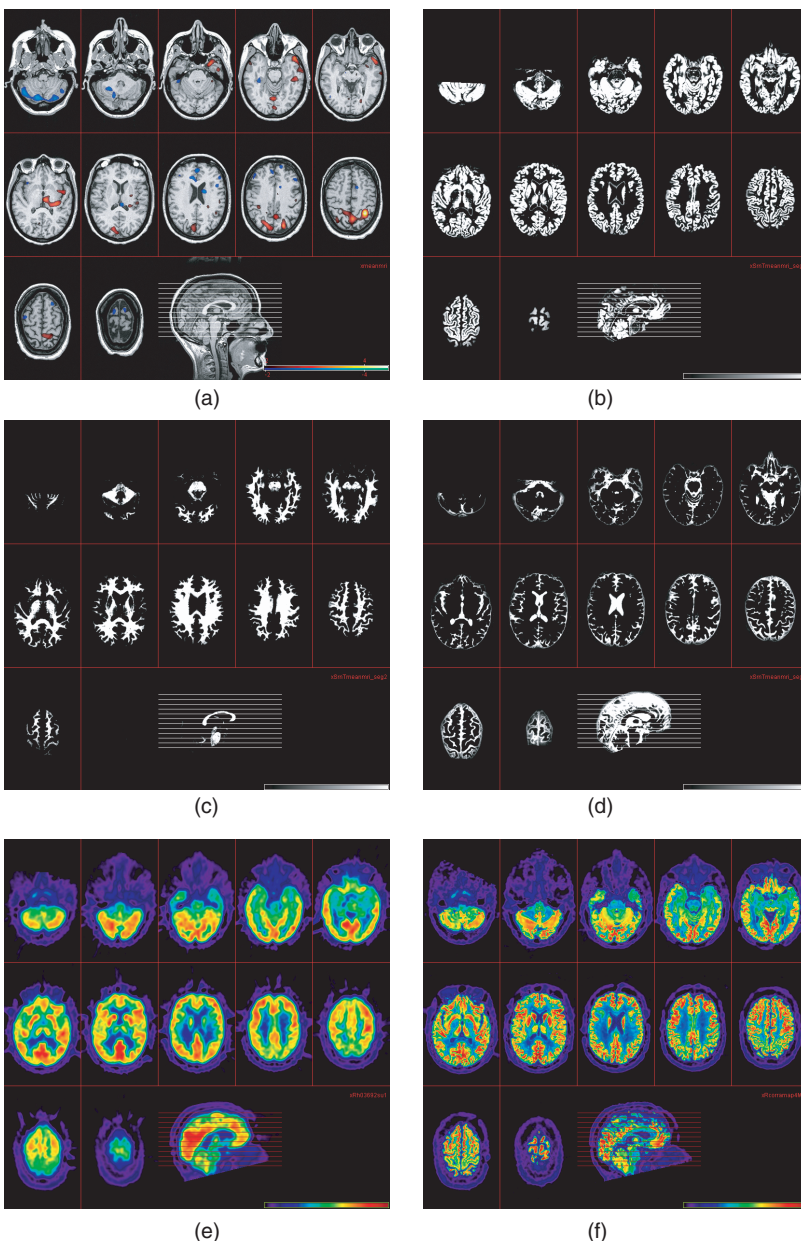


**Figure 5.9** (a)  $T_1$  MRI image of the brain with overlaid color subtraction SPECT (i.e., ictal minus interictal). The colored patterns are potential indications of epileptic activity. An ictal SPECT shows the brain perfusion during and an interictal SPECT in between epileptic seizures. (b,c,d) Segmented images of respectively the gray matter, white matter and CSF. (e) PET image obtained by conventional reconstruction. (f) PET image obtained by anatomy based MAP reconstruction. (Courtesy of Dr. K. Baete, Department of Nuclear Medicine.)

## 3D reconstruction

In SPECT with parallel hole collimation and in 2D PET the reconstruction problem is two dimensional and the above methods can be applied directly. However, there exist acquisition configurations that do not allow the problem to be reduced to a slice-by-slice reconstruction without approximations.

- There are many different geometries of mechanical collimators in SPECT. One example is the cone-beam collimator. It has a single focal point. Hence, all the projection lines that arrive at the 2D detector intersect in this point, and exact reconstruction from cone-beam data requires true 3D methods.
- In 3D PET all possible projection lines that intersect the detector surface (coincidence lines) are

used, both parallel and oblique to the transaxial plane. This 3D acquisition has the advantage that more data are obtained from each radioactive pixel, thus reducing the noise.

In these cases, the reconstruction program needs to compute the entire volume using all data simultaneously. This is often called true 3D reconstruction. Three currently used 3D reconstruction approaches are discussed below.

### Filtered backprojection

Filtered backprojection can be extended to true 3D reconstruction for PET. This is only possible if the sequence of projection and backprojection results in a shift-invariant point spread function. That is only true if every point in the reconstruction volume is intersected by the same configuration of measured projection lines, which is not the case in practice. Points near the edge of the field of view are intersected by fewer measured projection lines. In this case, the data may be completed by computing the missing projections as follows. First, a subset of projections that meets the requirement is selected and reconstructed to compute an initial, relatively noisy, reconstruction image. Next, this reconstruction is forward projected along the missing projection lines to compute an estimate of the missing data. Then, the computed and measured data are combined into a single set of data that now meets the requirement of shift-invariance. Finally, this completed dataset is reconstructed with true 3D filtered backprojection.

### ML reconstruction

The ML approach can be applied to the 3D dataset directly. The formulation is very general, and the coefficients  $c_{ij}$  in Eq. (5.20) can be used to describe true 3D projection lines. Because the number of calculations in each iteration increases with the number of projection lines, the computational burden becomes quite heavy for a true 3D reconstruction.

### Fourier rebinning

Fourier rebinning converts a set of 3D data into a set of 2D projections. It is based on a property of the Fourier transform of the sinograms. It has also been shown that the Poisson nature of the data is more or less preserved. The resulting 2D set can then be reconstructed with the 2D ML-EM algorithm. In practice, however, the exact rebinning algorithm is not used. Instead, an approximate expression is employed

because it is much faster and is sufficiently accurate for most configurations.

## Image quality

### Contrast

The contrast is mainly determined by the characteristics of the tracer and the amount of scatter. The specificity of a tracer for a particular metabolic process is usually not 100%. For example, for most tracers the blood concentration decreases rapidly but is typically not zero during the study. Consequently, the blood concentration produces a “background” tracer uptake, which decreases the contrast. Scattered photons also produce a background radiation that reduces the contrast.

### Spatial resolution

In nuclear medicine the resolution is mostly expressed as the full width at half maximum (FWHM) of the PSF.

In PET, the overall FWHM in the reconstructed image is about 4 to 8 mm. The spatial resolution is mainly limited by the following factors.

- *The positron range* A positron can only annihilate when its kinetic energy is sufficiently low. While reducing its energy by collisions with the electrons of surrounding atoms, the positron travels over a certain distance. The average distance depends on the isotope and is on the order of 0.2 to 2 mm.
- *The deviation from 180°* The annihilation photons are not emitted in exactly opposite directions. There is a deviation of about 0.3°, which corresponds to 2.8 mm for a camera of 1 m diameter.
- *The detector resolution* This is often called the “intrinsic” resolution. The size of the individual detector crystals is currently about 4 mm × 4 mm. This limits the intrinsic resolution to about 2 to 3 mm. If the detection is done with a single large crystal, the resolution is usually about 4 mm.

In SPECT, the overall FWHM in the reconstructed image is about 1 to 1.5 cm. The spatial resolution is affected by the following.

- *The detector resolution* This is comparable to PET.
- *The collimator resolution* The collimator is designed to select photons that propagate along a thin line. However, it has finite dimensions and, as

a result, it accepts all the photons that arrive from within a small solid angle. Therefore, the FWHM of the PSF increases linearly with increasing distance to the collimator. At 10 cm, the FWHM is on the order of 1 cm, and in the image center around 1.5 cm. The collimator resolution dominates the SPECT spatial resolution.

## Noise

We have already seen that Poisson noise contributes significantly to the measurements. The ML-EM reconstruction algorithm takes this into account and inherently limits the influence of this noise by terminating the procedure after a few tens of iterations.

Another noise factor is due to Compton scatter. It produces a secondary photon that is deflected from the original trajectory into a new direction. Some of the scattered photons reach the detector via this broken line. Such a contribution to the measurement is undesired, and a good camera suppresses this as much as possible. The system can reject scattered photons based on their energy. As compared to primary photons, the scattered photons have a lower energy, which is measured by the detector electronics. However, the energy resolution is finite (10% for Na(Tl)), and some of the scatter is unavoidably accepted. The remaining scatter has a negative effect on the image contrast and the accuracy of quantitative measurements.

## Artifacts

There are many possible causes of artifacts in SPECT and PET. Malfunction of the camera is an important cause and quality control procedures are mandatory to prevent this. However, some artifacts are inherent to the imaging and reconstruction process. The most important influencing factors are attenuation, scatter, noise, and patient motion.

- **Attenuation** Accurate correction for attenuation is only possible if a transmission scan is available. Previously, in stand-alone PET, these were obtained by rotating line sources containing the positron-emitting germanium. This procedure was time consuming and was not performed in some centers. The reconstruction process then assumes that there is no attenuation, which yields severe artifacts. A striking artifact in images which are not corrected for attenuation is the apparent high tracer uptake in the lungs and the skin. There will also be a nonhomogenous distribution in organs

in which the real distribution is homogenous. In modern combined PET/CT scanners, a whole-body CT scan is obtained and used to construct a 511 keV attenuation map which is used for attenuation correction. This correction might introduce artifacts by itself, specifically if there is a misalignment between the emission data and the CT. Figure 5.10 shows a coronal slice of a whole-body study reconstructed without and with attenuation correction. The study was done to find regions of increased FDG uptake (“hot spots”). Although both images clearly show the hot spots, the contours of the tumor and organs are less accurately defined in the study without attenuation correction. A striking artifact in Figure 5.10(a) is the apparent high tracer uptake in the lungs and the skin.

- **Compton scatter** Scattered photons yield a relatively smooth but nonuniform background uptake.
- **Poisson noise** Using filtered backprojection the statistical noise yields streak artifacts, comparable to those in CT (see Figure 3.21(b)). Iterative reconstruction (p. 112) on the other hand tends to keep the spatial extent of such artifacts quite limited.
- **Patient motion** SPECT and PET are more subject to patient motion than the other imaging modalities because of the longer acquisition time. Pure blurring because of motion appears only if all the projections are acquired simultaneously (i.e., in PET without preceding transmission scan). In attenuation-corrected PET, patient motion destroys the required registration between the emission and transmission data, which results in additional artifacts at the edges of the transmission image (Figure 5.10(c)). In SPECT, patient motion yields inconsistent projections and severe artifacts as well. Many researchers have investigated motion correction algorithms, but the problem is difficult, and so far no reliable method has emerged that can be applied in clinical routine.

## Equipment

### Gamma camera and SPECT scanner

Most gamma cameras use one or more large NaI(Tl) crystals (Figure 5.11). A lead collimator is positioned in front of the crystal. It collimates and also protects the fragile and very expensive crystal. Note, however, that the collimator is fragile as well, and the thin lead

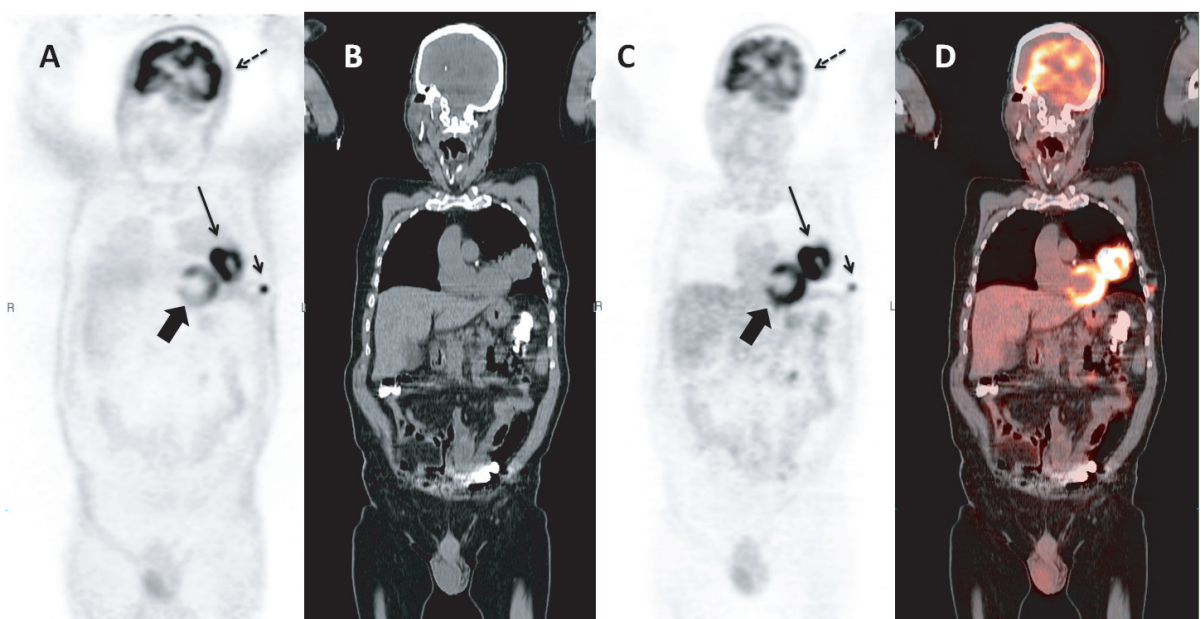


**Figure 5.10** Coronal slice of a whole-body PET/CT study reconstructed without (a) and with (c) attenuation correction based on whole-body CT (b). The relative intensity of the subcutaneous metastasis (small arrow) compared to the primary tumor (large arrow) is much higher in the noncorrected image than in the corrected one, because the activity in this peripheral lesion is much less attenuated than the activity in the primary tumor. A striking artifact in (a) is the apparent high uptake in the skin and the lungs. Note also that regions of homogenous uptake, such as the heart (thick arrow), are no longer homogenous, but show a gradient. Attenuation correction can lead to artifacts if the correspondence between the emission and transmission data is not perfect. The uptake in the left side of the brain (dotted arrow) is apparently lower than in the contralateral one in (c). The fused data set (d) representing the attenuation-corrected PET image registered on the CT image shows that the head did move between the acquisition of the CT and the emission data, resulting in an apparent decrease in activity in the left side of the brain. Courtesy of the Department of Nuclear Medicine



**Figure 5.11** (a) Gamma camera and SPECT scanner with two large crystal detectors. (b) System with three detector heads. If the gamma camera rotates around the patient it behaves like a SPECT scanner. Today, the difference between gamma units and SPECT systems has therefore become rather artificial. (Courtesy of the Department of Nuclear Medicine.)

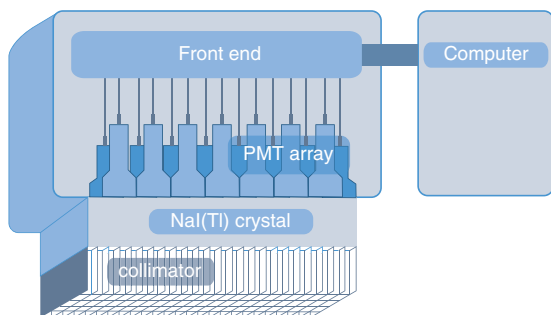


**Figure 5.12** Schematic representation of a gamma camera with a single large scintillation crystal ( $52 \times 37\text{ cm}$ ) and parallel hole collimator.

septa are easily deformed. At the other side of the crystal, an array of PMTs is typically attached to it. Front end electronics interface this PMT array to the computer (Figure 5.12).

For SPECT the detectors are mounted on a flexible gantry (Figure 5.11) since they must rotate over at least  $180^\circ$  around the patient. In addition, the detectors must be as close to the patient as possible because the spatial resolution decreases with the distance from the collimator. Obviously, the sensitivity is proportional to the number of detector heads, and the acquisition time can be decreased with increasing number of detector heads. For some examinations, the body part is too large to be measured in a single scan. Similar to CT, the computer then controls the table and slowly shifts the patient to scan the complete volume.

A camera cannot detect more than one photon at a time, because all PMTs together contribute to that single detection. From the PMT outputs, the front end electronics calculate four values, usually called  $x$ ,  $y$ ,  $z$ , and  $t$ .

- $(x, y)$  are the position coordinates. They are computed using Eq. (5.14).
- $z$  is a measure of the photon energy and is computed as  $\sum_i S_i$ . Because the PMT output is a pulse with a duration of a few hundred nanoseconds,  $S_i$  is the integration of this pulse over time:  $S_i = \int_{t_0}^{t_1} s_i(t) dt$ .

The energy  $z$  of detected photons is compared with an energy window  $[z_{\min}, z_{\max}]$ , which depends on the tracer used. If  $z > z_{\max}$ , two or more photons hit the crystal simultaneously, messing up the computation of  $(x, y)$ . If  $z < z_{\min}$ , the photon is due to Compton scatter and must be discarded.



**Figure 5.13** PET scanner. A movable table shifts the patient through the circular hole in the gantry. The external design is similar to that of a CT scanner and to some extent to that of an MRI scanner. (Courtesy of the Department of Nuclear Medicine.)

Some tracers emit photons at two or a few different energy peaks. In this case, multiple energy windows are used.

- $t$  is the detection time and is computed as the moment when the integration of  $\sum_i \int_{t_0}^t s_i(t) dt$  reaches a predefined fraction of  $z$ .

## PET scanner

Most PET cameras (Figure 5.13) consist of a complete ring (diameter  $\approx 1\text{ m}$ ) of BGO, GSO or LSO crystal modules. In PET, no detector rotation is therefore required. Table motion, however, may still be needed and is comparable to that of a gamma camera.

The detectors are typically small scintillation crystals (e.g.,  $4\text{ mm} \times 4\text{ mm}$ ) glued together in modular 2D arrays (e.g.,  $13 \times 13$ ) and connected to PMTs (e.g.,  $2 \times 2$ , a few centimeters width each). These modules are packed on a ring around the field of view. A PET scanner can contain multiple neighboring rings of modules, this way increasing the axial field of view. For example, three rings of  $13 \times 4\text{ mm}$  each yield an axial FOV of about  $16\text{ cm}$ .

The computation of the crystal coordinates  $(x, y)$ , the energy  $z$  and the time  $t$  is comparable to that for a large single-crystal detector but is restricted to a single module. This way multiple photons can be detected at the same time by different crystal modules. The detection time  $t$  is determined with an accuracy in the range of 1 to 10 ns (in 1 ns light travels about 30 cm), which is

short as compared to the scintillation decay constant\* (300 ns for BGO, 30–60 ns for GSO and 40 ns for LSO; 230 ns for NaI(Tl) in SPECT). The events are discarded only if a single photon is detected or if more than two photons hit the camera within the uncertainty interval. For example, if two photon pairs arrive simultaneously (i.e., within the coincidence timing resolution) at four different modules, they are rejected. Note that, if two photons are detected by the same module within the scintillation decay interval, they are also rejected. This last situation, however, does not happen frequently because of the large amount of crystal modules.

An important problem is the presence of so-called *randoms*. Randoms are photon pairs that do not originate from the same positron but nevertheless hit the camera within the short time interval during which the electronic detection circuit considers this as a coincidence ( $\approx 1\text{--}10$  ns). The probability of a random increases with the square of the radioactivity and cannot be ignored. The number of randoms can be estimated with the *delayed window* technique, shown schematically in Figure 5.14. The camera counts the number of detected photon pairs that are obtained with a minimal delay. This short delay time is chosen sufficiently large to guarantee that the two photons do not belong to a single annihilation. This number of guaranteed randoms can be considered independent of the time delay. Consequently, the same amount of randoms can be assumed to appear

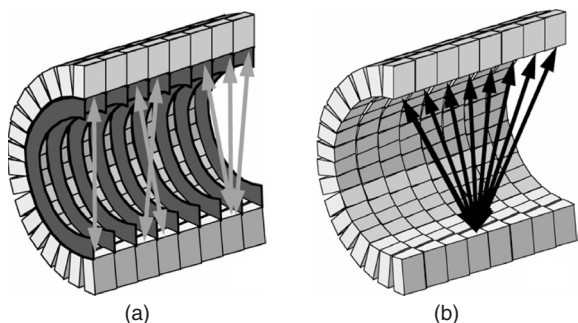


**Figure 5.15** Schematic representation of a PET detector ring cut in half. (a) When septa are in the field of view, the camera can be regarded as a series of separate 2D systems. (b) Retracting the septa increases the number of projection lines and hence the sensitivity of the system, but true 3D reconstruction is required.

during the measurement of true annihilation pairs and must be subtracted in order to calculate the true coincidences.

Older PET cameras are usually equipped with retractable septa (see Figure 5.15(a)). When the septa are in the field of view, the camera operates in the so-called “2D-mode,” and the detector is considered to be a concatenation of independent rings. Only projection lines within parallel planes can be accepted, as the septa absorb photons with oblique trajectories. Recent systems do not contain septa and all the available projection lines are accepted (see Figure 5.15(b)). Reconstruction from these data requires true 3D reconstruction algorithms.

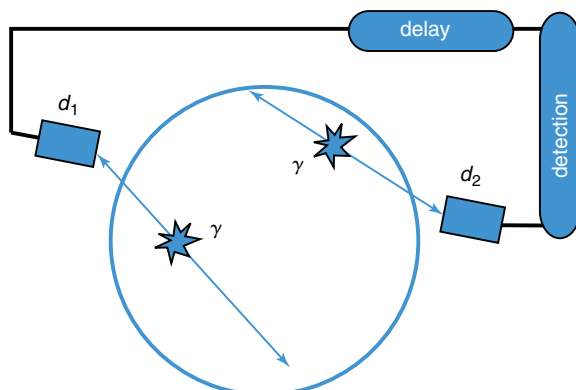


**Figure 5.14** Schematic representation of a random and its detection. One of the two photons is detected with a small time delay.

\* Time constant assuming exponential decay, i.e., the moment when the light intensity has returned to  $e^{-1}$  of its maximum value.

## Hybrid systems

PET and SPECT systems can be combined with a CT or even a MR system. Among these combinations, the PET/CT system (Figure 5.16) is currently the most popular and has become quite common in clinical practice. In this case the CT image is used for attenuation correction. A potential problem is the registration mismatch between the transmission and the emission image due to patient motion during the long duration of the examination (half an hour and more). Nonrigid registration may offer a solution (see Chapter 7, p. 183) but is not straightforward. Another, technical, problem is due to the energy dependence of the linear attenuation coefficient. In PET, for example, the photon energy is 511 keV while an X-ray source in CT transmits an energy spectrum with a maximum energy defined by the tube voltage. For example, a tube with a voltage of 140 kV yields X-ray photons



**Figure 5.16** A CT and a PET system are linked and integrated into a single gantry and share a common patient bed. Two hybrid PET/CT scanners are shown here. (Courtesy of the Department of Nuclear Medicine.)

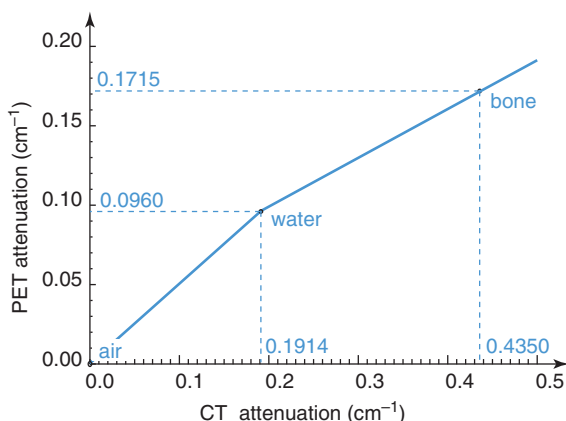


**Figure 5.17** Approximate relationship between the linear attenuation coefficient in CT, operating at 140 kV, and PET. The energy spectrum of the X-ray photons is approximated by a single effective energy of 70 keV. The energy of the PET photons is 511 keV. Tissue is assumed to be a linear mixture of either air and water, or water and bone. The result is a piecewise linear conversion function.

with energy 140 keV and lower. To calculate the attenuation coefficient for the emission image, the X-ray energy spectrum is typically approximated by a single average or *effective* energy. For example, for a voltage of 140 kV the maximum X-ray photon energy is 140 keV and the effective energy is assumed to be 70 keV. Furthermore, the relationship between the attenuation coefficient at 70 keV and at 511 keV is assumed to be piecewise linear (Figure 5.17).

### Time-of-flight (TOF) PET

If the uncertainty in measuring the difference in arrival times of a photon pair is limited to 1 ns or less, it becomes interesting to use this time difference to localize the position of the annihilation along the *line of response* (LOR). The uncertainty  $\Delta x$  in the position along the LOR can be calculated from the uncertainty  $\Delta t$  in measuring the coincidence, that is,

$$\Delta x = \frac{1}{2}c \Delta t. \quad (5.30)$$

More specifically,  $\Delta t$  and  $\Delta x$  are the FWHM of the uncertainty distributions in time and space respectively (Figure 5.18). A coincidence timing uncertainty  $\Delta t$  of 600 ps, for example, yields a positional uncertainty  $\Delta x$  of 9 cm along the LOR. Further reducing  $\Delta t$  to 100 ps reduces this positional uncertainty  $\Delta x$  to 1.5 cm. This information can be fed to the reconstruction algorithm to improve the image quality. Indeed, instead of knowing that the annihilation took place somewhere along the LOR, the expected position along that LOR can now be expressed within a range defined by the spatial uncertainty distribution (FWHM =  $\Delta x$ ).

TOF PET requires proper reconstruction tools. Although ML-based statistical reconstruction can still be used, other algorithms have been developed such as 3D list-mode TOF reconstruction and algorithms that place the events directly into the image space rather

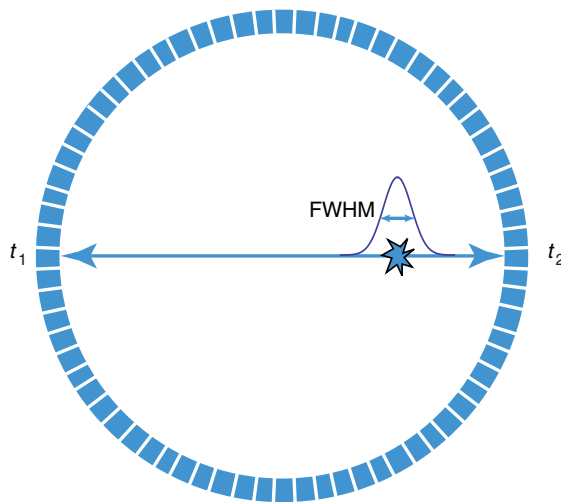


**Figure 5.18** Principle of TOF PET. The position of the annihilation can be calculated from the difference between the arrival times of both photons. The uncertainty in measuring this time difference can be represented by a statistical distribution with  $\text{FWHM} = \Delta t$ . The relationship between  $\Delta t$  and  $\Delta x$  (FWHM of the spatial uncertainty distribution) is given by Eq. (5.30).

than into the projection space. This theory was pioneered in the 1980s and has recently resurged due to the improvements in detector materials (LSO, LYSO, LaBr<sub>3</sub>) and electronic stability. A detailed discussion of these advances, however, is beyond the scope of this textbook.

### Clinical use

Nuclear medicine is based on the tracer principle. Small amounts of radioactive-labeled molecules are administered to measure functional parameters of different organs selectively (e.g., perfusion, metabolism, innervation). Many different tracers exist, and the number is still increasing. While gamma cameras need gamma-emitting tracers, PET needs positron emitters. Single-photon emitting atoms tend to be quite heavy. Typical organic molecules do not contain such atoms and must therefore be modified by binding the radioactive atom to the organic molecule. Most molecules are labeled with <sup>99m</sup>Tc (half-life 6 hours) because it is inexpensive and has ideal physical characteristics (short half-life; daughter of <sup>99</sup>Mo, which has a half-life of 66 hours and is continuously available; ideal  $\gamma$ -ray energy of 140 keV, which is high enough to leave the body but not too high to penetrate the crystal). Other important  $\gamma$ -emitting radionuclides are <sup>123</sup>I

(half-life 13 hours), <sup>131</sup>I (half-life 8 days), <sup>111</sup>In (half-life 3 days), <sup>201</sup>Tl (half-life 3 days), and <sup>67</sup>Ga (half-life 3 days). Positron emitting tracers are light, have a short half-life, and can be included in organic molecules without modifying their chemical characteristics. The most used in nuclear medicine are <sup>11</sup>C (half-life 20 min), <sup>13</sup>N (half-life 10 min), <sup>15</sup>O (half-life 2 min), and <sup>18</sup>F (half-life 109 min). With the exception of <sup>18</sup>F they have to be produced by a cyclotron in the hospital because of their short half-life.

The most important clinical applications in nuclear medicine are studies of bone metabolism, myocardial perfusion and viability, lung embolism, tumors, and thyroid function.

- **Bone metabolism** For the exploration of bone metabolism a <sup>99m</sup>Tc labeled phosphonate can be used. It accumulates in proportion to bone turnover, which is increased by several pathologies, such as tumors, fractures (Figure 5.19), inflammations, and infections. A SPECT/CT scanner, combining metabolic information of the SPECT and anatomic information of the CT, further improves the diagnostic accuracy of bone disorders.

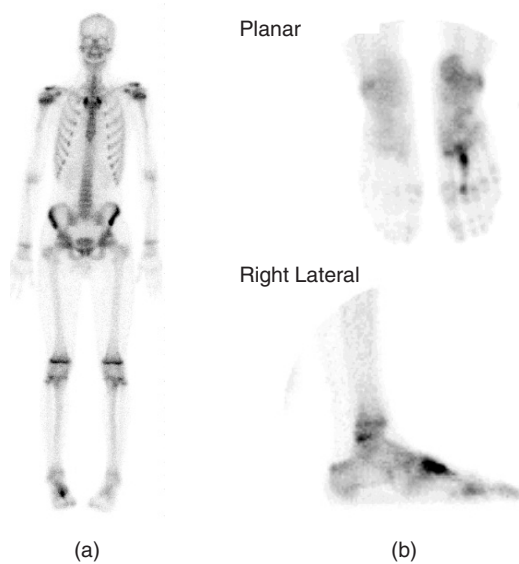


**Figure 5.19** Left: whole-body scintigraphy after injection of 25 mCi <sup>99m</sup>Tc-labeled methylene diphosphonate. This patient suffers from a stress fracture of the right foot. Right: control scans show an increased uptake in the metatarsal bone II compatible with a local stress fracture. (Courtesy of Professor L. Mortelmans, Department of Nuclear Medicine.)

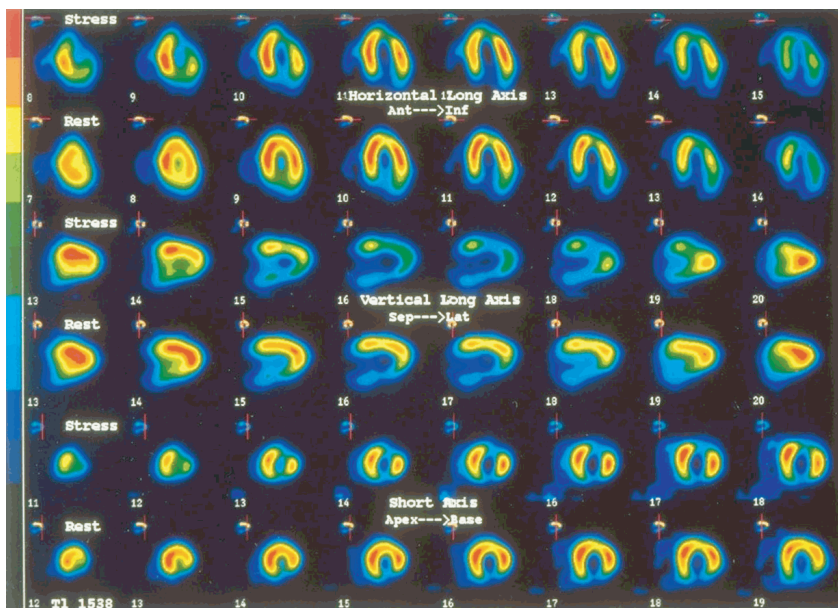


**Figure 5.20** Myocardial perfusion SPECT scan. Rows 1, 3, and 5 show the myocardial perfusion during a typical stress test. Rows 2, 4, and 6 show the rest images acquired 3 hours later. The first two rows are horizontal long-axis slices, the middle two rows are vertical long-axis slices, and the bottom two rows are short-axis slices. This study shows a typical example of transient hypoperfusion of the anterior wall. On the stress images, there is a clear perfusion defect on the anterior wall (horizontal-axis slice 9, vertical long-axis 16 to 18, short-axis slice 13 to 18). The perfusion normalizes on the corresponding rest images. (Courtesy of Professor L. Mortelmans, Department of Nuclear Medicine.)

- **Myocardial perfusion and viability** For myocardial perfusion, tracers are used that are accumulated in the myocardium in proportion to the blood flow. Examples of such tracers are the  $\gamma$ -emitting tracers  $^{201}\text{Tl}$  and  $^{99\text{m}}\text{Tc}$ -Mibi, and the PET tracers  $^{13}\text{NH}_3$  and  $\text{H}_2^{15}\text{O}$ . The choice of the imaging modality and tracer depends on factors, such as half-life, image quality, cost, and availability. Often, the imaging process is repeated after several hours to compare the tracer distribution after stress and at rest (Figure 5.20). This procedure answers the question whether there is a transient ischemia during stress. By comparing myocardial perfusion with glucose metabolism, PET is the gold standard to evaluate myocardial viability.
- **Lung embolism** In order to detect lung embolism,  $^{99\text{m}}\text{Tc}$ -labeled human serum albumin is injected intravenously. This tracer with a mean diameter of 10–40  $\mu\text{m}$  sticks in the first capillaries it meets (i.e., in the lungs). Areas of decreased or absent tracer deposit correspond to a pathological perfusion, which is compatible with a lung embolism. The specificity of the perfusion scan can be increased by means of a ventilation scan

(Figure 5.21). Under normal conditions a gas or an aerosol with  $^{99\text{m}}\text{Tc}$ -labeled particles is spread homogeneously in the lungs by inhalation. Lung embolism is typically characterized by a mismatch (i.e., a perfusion defect with a normal ventilation). A perfusion CT scan of the lungs has become the first choice technique for diagnosis of lung embolism.

- **Tumors** A very successful tracer for measuring metabolic activity is  $^{18}\text{FDG}$  (fluoro-deoxy-glucose). This molecule traces glucose metabolism. The uptake of this tracer is similar to that of glucose. However, unlike glucose, FDG is only partially metabolized and is trapped in the cell. Consequently, FDG accumulates proportionally to glucose consumption. A tumor is shown as an active area or “hot spot” (Figure 5.22), as in most tumors glucose metabolism is considerably higher than in the surrounding tissue. Whole-body FDG has become a standard technique for the staging of oncologic patients and also for the therapeutic evaluation of chemotherapy and/or radiotherapy.
- **Thyroid function** Captation of  $^{99\text{m}}\text{Tc}$  pertechnetate or  $^{123}\text{I}$  iodide shows the tracer distribution

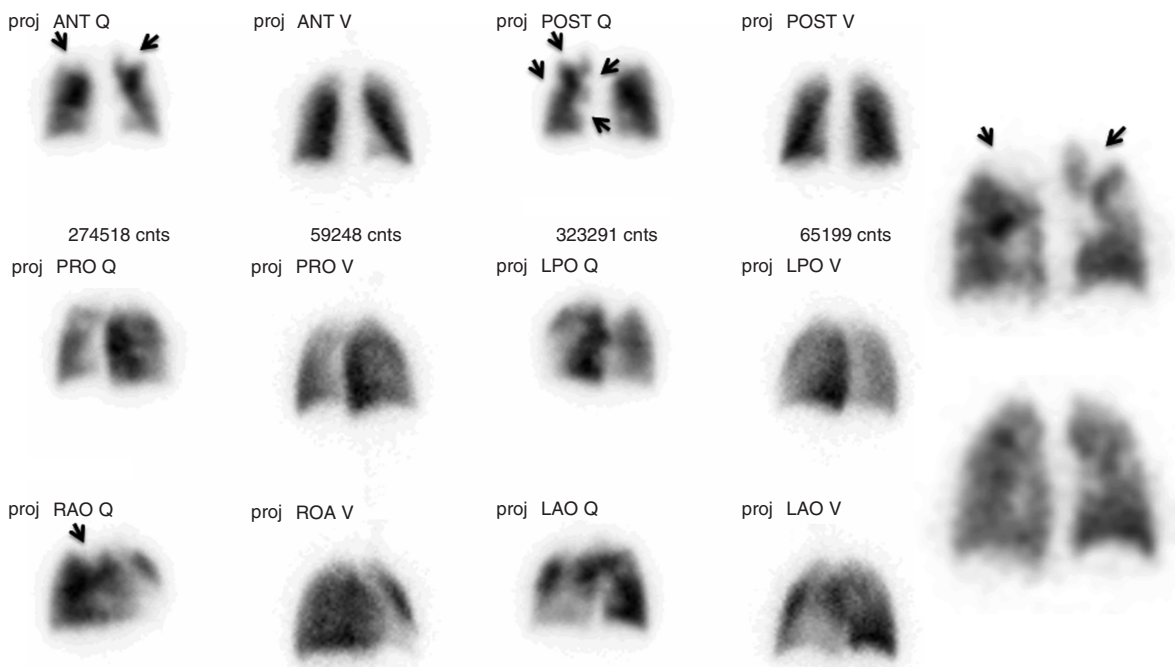


**Figure 5.21** Lung perfusion (Q) and ventilation (V) scan. The second and fourth columns show six planar projections of a ventilation SPECT scan obtained after the inhalation of radioactive pertechnegas distributed homogeneously throughout both lungs. The first and third columns show the corresponding lung perfusion images obtained after injection of  $^{99m}\text{Tc}$ -labeled macroaggregates. Several triangular-shaped defects (arrows) are visible in the perfusion scan with a normal ventilation at the same site. This mismatch between perfusion and ventilation is typical for lung embolism. The fifth column shows a coronal section of the SPECT data set with triangular defects (arrowheads) in the perfusion (upper row) and a normal ventilation (lower row). (Courtesy of Professor L. Mortelmans, Department of Nuclear Medicine.)

within the thyroid, which is a measure of the metabolic function (Figure 5.23).  $^{131}\text{I}$  iodide with a half-life of 8 days is mainly used for treatment of hyperthyroidism (thyroid hyperfunction) or thyroid cancer.

- **Neurological disorders** Brain disorders can be diagnosed using SPECT perfusion scans and PET FDG scans measuring brain metabolism. FDG PET brain scans play an important role in the early and differential diagnosis of dementia (Figure 5.24). New tracers are used for the evaluation of neuromodulators, transporters, enzymes, etc., allowing more specific diagnosis of several brain disorders. A typical example is the presynaptic dopamine transporter (DAT) scan, measuring the amount of dopamine-producing cells in the substantia nigra and facilitating early and differential diagnosis of Parkinson disease, possibly in combination with postsynaptic dopamine receptor (D2) imaging (Figure 5.25).

## Biologic effects and safety

Unfortunately, tracer molecules are not completely specific for the investigated function and are accumulated in other organs, such as the liver, the kidneys, and the bladder. Furthermore, the radioactive product does not disappear immediately after the imaging procedure but remains in the body for hours or days after the clinical examination is finished. The amount of radioactivity in the body decreases with time because of two effects.

- **Radioactive decay** This decay is exponential. Every half-life, the radioactivity decreases by a factor of two.
- **Biologic excretion** Many tracers are metabolized, and the biologic excretion is often significant as compared with the radioactive decay. It can be intensified with medication. This also means that the bladder receives a high radiation dose, which can

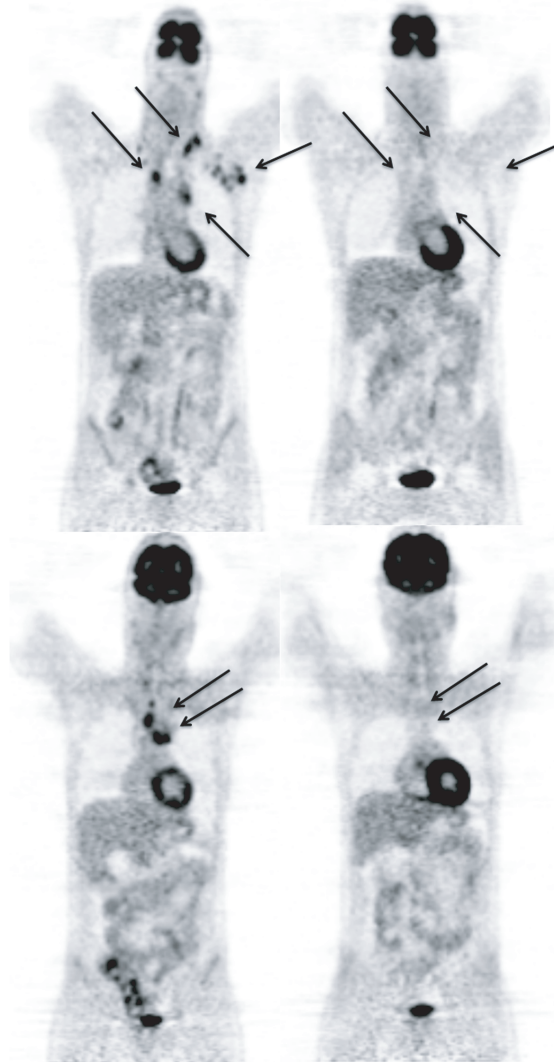


**Figure 5.22**  $^{18}\text{FDG}$  PET scan of a patient suffering from a lymphoma in the mediastinum and the left axilla (left column). The pathological  $^{18}\text{FDG}$  uptake in the lymphomatous lymph nodes (arrows) disappeared after chemotherapy (right column). (Courtesy of Professor L. Mortelmans, Department of Nuclear Medicine.)

amount to more than 50% of the patient's effective dose.

The radiation exposure of a particular organ is a function of the activity in the entire body. Simulation software exists that is based on models for the human body (e.g., the *MIRD model* (medical internal radiation dosimetry) of the Society of Nuclear



**Figure 5.23**  $^{99\text{m}}\text{Tc}$  pertechnetate thyroid scan of a patient with a multinodular goiter. The irregularly enlarged thyroid is delineated. Several zones of normal and increased uptake are visible. Hyperactive zones are seen in the upper and lower pole of the right thyroid lobe. In the right interpolar region there is a zone of relative hypoactivity. (Courtesy of Professor L. Mortelmans, Department of Nuclear Medicine.)

Medicine). Initial tracer concentrations, tracer accumulation, and excretion times must be entered in the simulator, which then computes the radiation load to each organ and derives the effective dose in millisieverts. For the input data, typical values can be used. These values can be defined by repeatedly scanning an injected subject until the radioactivity becomes negligible. Typical doses for a large number of tracers are published by the International Commission on Radiological Protection (ICRP). For example, the effective patient doses of a study of the lung are 0.1–0.5 mSv, the thyroid 0.4–0.7 mSv, bone 1.3 mSv, the myocardium around 5 mSv, and tumors studied with FDG around 6 mSv and gallium 13.0 mSv. Roughly speaking, they have the same order of magnitude as the effective doses for diagnostic radiographic imaging (see p. 31) or CT (see p. 59).

For the patient's entourage, for example the personnel of the nuclear medicine department, it is important to take into account that the radiation dose decreases with the square of the distance to the source and increases with the exposure time. It is therefore recommended that medical personnel stay at a certain distance from radioactive sources, including the patient. Contamination of tracers must be avoided.

## Future expectations

Although continuous technical improvements can be expected (improved TOF and hybrid systems, new detectors, removal of motion artifacts, etc.)

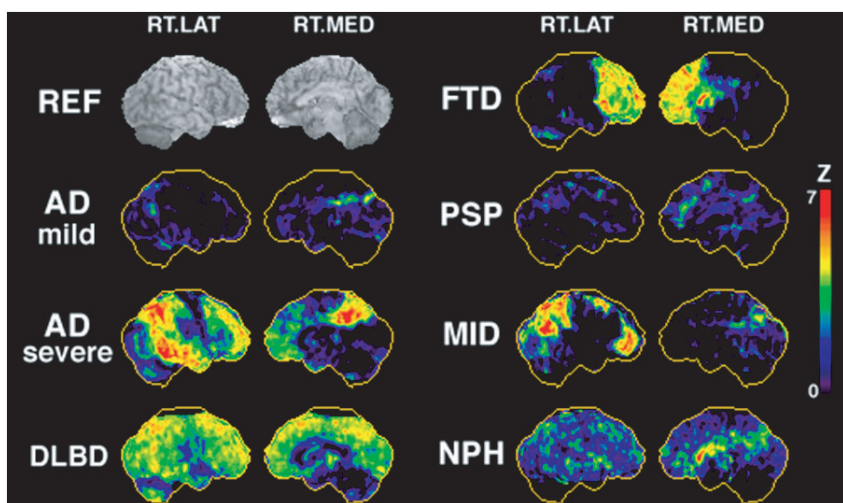


**Figure 5.24** Deviation of FDG uptake with respect to a normal database for different types of “dementias.” In the upper left corner, an anatomical MR reference image is shown. AD Alzheimer disease; DLBD Lewy body disease; FTD frontal lobe dementia; PSP progressive supranuclear palsy; MID multi infarct dementia; NPH normal pressure hydrocephalus. (Courtesy of Professor K. Van Laere, Department of Nuclear Medicine.)

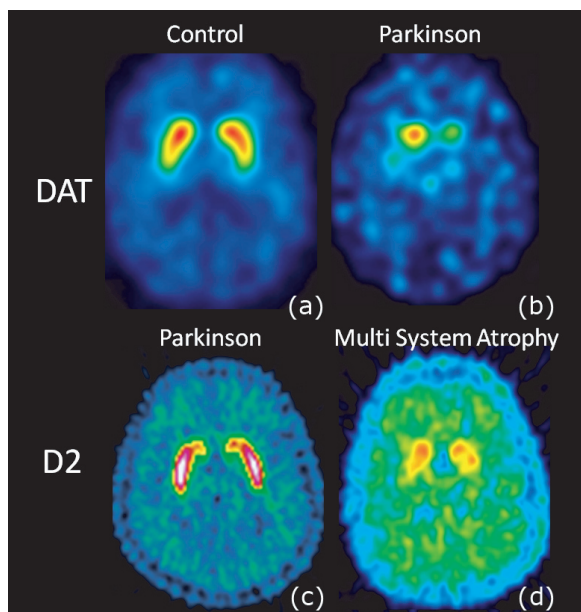


**Figure 5.25** Upper row:  $^{123}\text{I}$ -FP-CIT SPECT scan for presynaptic dopamine transporter (DAT) imaging. Lower row:  $^{11}\text{C}$ -raclopride PET scan for postsynaptic dopamine receptor (D2) imaging. (a) Healthy subject. (b,c) In an early Parkinson patient a decrease of the dopamine transporter (DAT) is seen in the basal ganglia while the postsynaptic dopamine receptor (D2) is still normal. (d) Parkinson patient with multi-system atrophy (MSA). The postsynaptic part of the dopaminergic synapse is also impaired. (Courtesy of Professor K. Van Laere, Department of Nuclear Medicine.)

progression will particularly be stimulated by the development of new generations of tracers.

More clinical indications will be created by labeling new compounds with PET tracers. There is a clear shift from rather aspecific tracers such as FDG to more specific biomarkers that bind to specific receptors. There are also new potentials for therapy with radioactive tracers, especially for the treatment of hematological diseases by means of radioimmunotherapy with labeled antibodies.

Medical imaging is further evolving towards the visualization of biological processes at the cell level. This way cellular function and molecular pathways in vivo can be studied, such as imaging of gene regulation, protein–protein interactions and stem cell tracking. This new discipline, which combines imaging with molecular biology, is called *molecular imaging*. It shifts the focus from imaging the anatomy and function of organs towards imaging the behavior and interaction of molecules. Early disease detection and tracking of gene therapy are among the future applications. Figure 5.26 shows the basic principle of imaging gene expression in vivo. Although this evolution is not limited to nuclear medicine, theoretically emission tomography has the largest potential due to the variety of tracers that can be

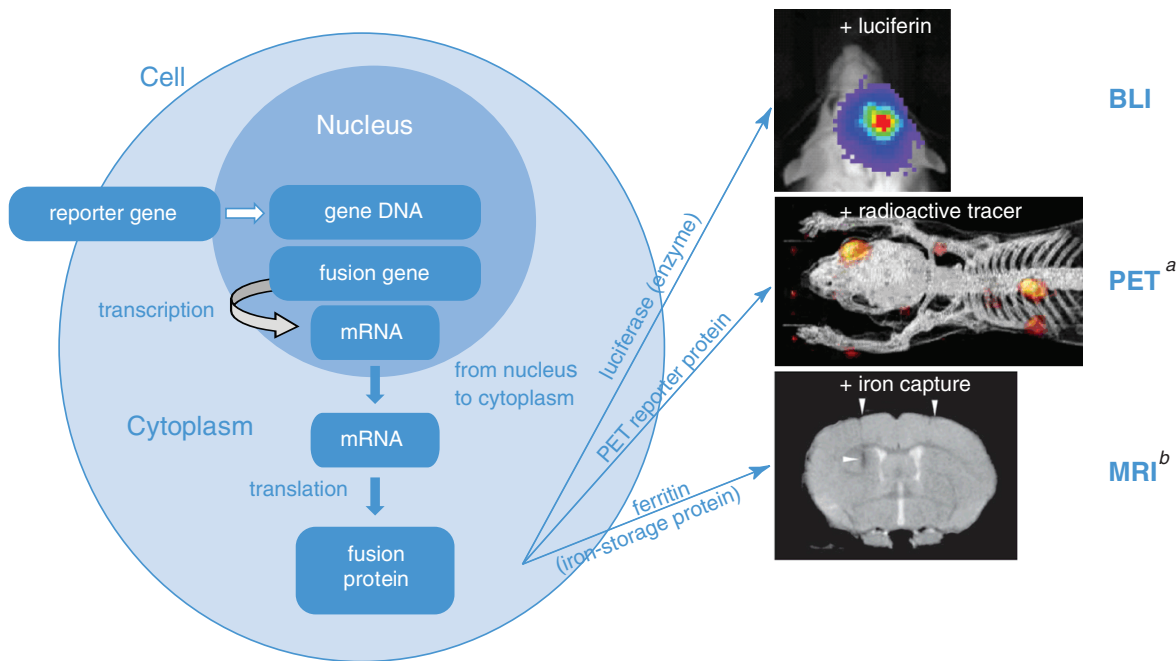


**Figure 5.26** Principle of molecular imaging. A reporter gene is attached to a gene of interest to create a gene fusion, which is copied (transcribed) into a messenger RNA (mRNA) molecule. The mRNA moves from the nucleus to the cytoplasm where its code is used during the synthesis of a protein (translation of mRNA into protein). Depending on the nature of the reporter gene the fusion protein is a reporter protein that is fluorescent (produces light), captures iron (visible in MRI) or interacts with a radioactive tracer (visible in SPECT or PET). (Courtesy of Prof. C. Deroose, Dept. of Nuclear Medicine.)

(<sup>a</sup>) Reprinted from G. Genove, U. DeMarco, H. Xu, W. F. Goins, and E. T. Ahrens. A new transgene reporter for in vivo magnetic resonance imaging, *Nature Medicine*, **11**(4): 450–454, 2005.

(<sup>b</sup>) Reprinted from C. M. Deroose, A. De, A. M. Loening, P. L. Chow, P. Ray, A. F. Chatzioannou, and S. S. Gambhir. Multimodality imaging of tumor xenografts and metastases in mice with combined small-animal PET, small-animal CT, and bioluminescence imaging, *Journal of Nuclear Medicine*, **48**(2): 295–303, 2007.

developed. Today most of these techniques are subject to fundamental research. Adapted systems have been developed for imaging small animals, such as

mice and rats, *in vivo*. Because of their small size these scanners are typically labeled with the prefix “micro” (micro-PET/SPECT/CT/MRI/US).